

# Detailed Cluster Mass and Light profiles of A1703, A370 & RXJ1347-11 from Deep Subaru Imaging<sup>\*</sup>

Elinor Medezinski,<sup>1†</sup> Tom Broadhurst,<sup>1</sup> Keiichi Umetsu,<sup>2</sup> Masamune Oguri,<sup>3</sup> Yoel Rephaeli<sup>1</sup> and Narciso Benítez<sup>4</sup>

<sup>1</sup>School of Physics and Astronomy, Tel Aviv University, Tel Aviv 69978, Israel

<sup>2</sup>Institute of Astronomy and Astrophysics, Academia Sinica, P. O. Box 23-141, Taipei 106, Taiwan, Republic of China

<sup>3</sup>Kavli Institute for Particle Astrophysics and Cosmology, Stanford University, 2575 Sand Hill Road, Menlo Park, CA 94025, USA

<sup>4</sup>Instituto de Astrofísica de Andalucía (CSIC), Granada, Spain

8 February 2010

## ABSTRACT

Weak lensing work can be badly compromised by unlensed foreground and cluster members which dilute the true lensing signal. We show how the lensing amplitude in multi-colour space can be harnessed to securely separate cluster members from the foreground and background populations for three massive clusters, A1703 ( $z = 0.258$ ), A370 ( $z = 0.375$ ) and RXJ1347-11 ( $z = 0.451$ ) imaged with Subaru. The luminosity functions of these clusters when corrected for dilution, show similar faint-end slopes,  $\alpha \simeq -1.0$ , with no marked faint-end upturn to our limit of  $M_R \simeq -15.0$ , and only a mild radial gradient. In each case, the radial profile of the  $M/L$  ratio peaks at intermediate radius,  $\simeq 0.2r_{vir}$ , at a level of  $300 - 500(M/L_R)_\odot$ , and then falls steadily towards  $\sim 100(M/L_R)_\odot$  at the virial radius, similar to the mean field level. This behaviour is likely due to the relative paucity of central late-type galaxies, whereas for the E/S0-sequence only a mild radial decline in  $M/L$  is found for each cluster. We discuss this behaviour in the context of detailed simulations where predictions for tidal stripping may now be tested accurately with observations.

**Key words:** cosmology: observations – cosmology: dark matter – gravitational lensing – galaxies: clusters: individual(Abell 1703) – galaxies: clusters: individual(Abell 370) – galaxies: clusters: individual(RX J1347.5-1145) – galaxies: luminosity function

## 1 INTRODUCTION

Galaxy Clusters are the largest virialised objects whose properties reflect the initial spectrum of density perturbations and the evolutionary history of dark matter (DM) and baryons. Wide ranging observations provide a wealth of information for examining the relation between dark and visible matter and their radial profiles. Unlike galaxies, where substantial cooling is predicted to have concentrated baryons in the centres of DM halos, clusters are observed to cool relatively inefficiently via thermal emission so that the gas remains close to the virial temperature, making cluster mass profiles easy to interpret, as corrections for gas cooling are not significant (Blumenthal et al. 1986; Broadhurst & Barkana 2008).

Lensing work is now able to achieve measurements of

projected cluster mass profiles with unprecedented detail, sufficient to usefully address the distinctive prediction of a relatively shallow mass profiles for CDM dominated halos (Navarro, Frenk & White, 1997, hereafter NFW; Duffy et al., 2008). Combined weak and strong lensing measurements have shown that the continuously steepening form of the NFW profile is a reasonable description for the mass profiles of three careful, independent studies (Kneib et al. 2003; Gavazzi 2005; Broadhurst et al. 2005), although with surprisingly high values derived for the profile concentration parameter in each case (Broadhurst et al. 2005). More recently, the concordance  $\Lambda$ CDM cosmology has been examined critically with a somewhat larger sample of clusters, indicating that the concentrations derived are significantly higher than predicted over a wide range of cluster mass, after accounting for statistical corrections for lensing-induced biases. This is seen both in terms of the size of the Einstein radius (Broadhurst & Barkana 2008; Oguri & Blandford 2009; Zitrin et al. 2009) and the weak lensing (WL) mass profiles of several well known clusters (Broadhurst et al. 2008; Sadeh & Rephaeli 2008; Lapi & Cavaliere 2009).

\* Based on data collected at Subaru Telescope and obtained from the SMOKA, which is operated by the Astronomy Data Center, National Astronomical Observatory of Japan.

† elinor@wise.tau.ac.il

Current detailed cluster mass and light profiles can now be used to examine the ratio of  $M/L$  all the way out to the virial radius. Comparisons of the general DM distribution with the galaxy distribution are potentially of great interest as the distribution of galaxies is thought to be influenced by significant tidal forces which may substantially modify massive galaxy halos reducing their masses (Ghigna et al. 1998, 2000; Colín et al. 1999; Springel et al. 2001; De Lucia et al. 2004; Gao et al. 2004; Nagai & Kravtsov 2005; Limousin et al. 2009). Mass loss calculated over Hubble time in  $\Lambda$ CDM predict losses of  $\sim 30\%$  for orbits extending to the virial radius, with typically a loss of  $\sim 70\%$  near cluster centres, so that the ratio of integrated galaxy mass to the general DM distribution falls steadily towards the cluster centre (Nagai & Kravtsov 2005).

Stars are not expected to be stripped significantly in these simulations because of their location deep in the central potential of a galaxy. Hence, for clusters the galaxy light should simply trace mass, assuming both are collisionless, so that a fairly constant  $M/L$  is expected (Gao et al. 2004; Nagai & Kravtsov 2005). The presence of high-mass galaxies in the inner core, resulting from both higher merger rates and the effect of dynamical friction, explains the reduced value of the integrated  $M/L$  ratio within a radius of  $\leq 200h^{-1}$  kpc for the highest mass clusters (Nagai & Kravtsov 2005; El-Zant, Shlosman & Hoffman 2001).

Reliable  $M/L$  profiles of galaxy clusters have begun to emerge recently based on dynamical (Rines et al. 2000, 2004) and lensing based methods (Medezinski et al. 2007). For the local cluster A576, a careful dynamically-based  $M/L$  profile has been obtained with caustic work by (Rines et al. 2000), who note a puzzling declining behavior, with a peak around  $M/L \sim 600M/L_B$  at  $r \sim 100h^{-1}$  kpc, declining to a limiting  $100M/L_B$ , at  $r \sim 1h^{-1}$  Mpc and beyond. Other dynamical estimates from stacking together samples of clusters also show this overall behavior, where the  $M/L$  ratio may peak around 10% of the virial radius (Katgert, Biviano & Mazure 2004) and declines thereafter (Rines et al. 2000, 2004).

Our earlier lensing based determination of the  $M/L$  profile of A1689 (Medezinski et al. 2007) shows behaviour similar to the above dynamical work, with a peak of  $M/L_B \sim 400(M/L)_\odot$  at  $r \sim 100h^{-1}$  kpc, and a steady decline to  $\sim 100M/L_B$  at the virial radius,  $r \sim 2h^{-1}$  Mpc (Medezinski et al. 2007). In the case of A576 (Rines et al. 2000) and in our own work on A1689 (Medezinski et al. 2007), careful corrections are made for the trend of  $M/L$  of the stellar population with cluster radius, using the measured colours of cluster member galaxies which favour predominately redder, earlier-type galaxies in the central region. In both these differing analyses the colour trend was found to be weak and not nearly sufficient to account for the measured variation of the  $M/L$  profile, leaving a puzzling result which is generally at odds with the known result that  $M/L$  is an increasing function of scale. Clearly, it is important to extend the investigation of the  $M/L$  profile to more clusters to examine the generality of our earlier work and to examine possible trends with other observables in a more statistically robust way.

Our previous work demonstrated the importance of carefully selecting a background population to avoid contamination by the lensing cluster. It is not sufficient to simply exclude a narrow band containing the obvious E/S0 se-

quence, following common practice, because the lensing signal of the remainder bluer objects is found to fall rapidly towards the cluster centre relative to the background of red lensed galaxies indicating that unlensed cluster members are present blueward of the sequence diluting the true lensing signal (Broadhurst et al. 2005). Due to this effect, many WL studies have underestimated the masses and concentrations of cluster mass profiles (Lu et al. 2009), a point now widely acknowledged (Limousin et al. 2007; Oguri et al. 2009; Okabe et al. 2009). This effect resolved the long standing discrepancy between the strong and WL effects, with the WL signal underpredicting the observed Einstein radius by a factor of  $\sim 2.5$  (Clowe & Schneider 2001; Bardeau et al. 2005), based only on a minimal rejection of obvious cluster members using one or two-band photometry. Red background galaxies behind clusters have since been explored carefully with deep wide-field spectroscopy by Rines & Geller (2008), who emphasize that the red population in their cluster data comprises exclusively background objects.

This lensing “dilution” effect may be turned to our advantage as a means of correcting the cluster population for background contamination, extending the work of Medezinski et al. (2007). Here we analyze very high quality Subaru images of A1703, A370, & RXJ1347-11 for which we have accurate WL measurements. For these clusters, a wider range of colours is available than for A1689, which we make full use here to improve the separation of cluster members from foreground and background populations using the colour-colour (CC) diagram and application of our dilution method. Using the dilution method has the advantage that it does not require the actual subtraction of background galaxies which introduces the inherent uncertainty caused by the clustering of the background signal and the attendant requirement for the accurate photometry of control fields.

In § 2 we present the cluster observations, the data reduction, and in § 3 we explain how we select cluster galaxies, background samples, and foreground samples. In § 4 we examine evolutionary tracks to reinforce the sample selection criteria, and compare with blank-field surveys to determine redshift distributions in § 5. In § 6 we describe the WL analysis, and in § 7 we describe how the WL measurements are used to determine the cluster fraction using our WL dilution method. In § 8 we derive the light profile of each cluster, and compare with the mass profile to obtain the  $M/L$  profile in § 9. In § 10 we investigate the shape and variation of the cluster luminosity functions (LF) and its radial dependence. Finally, we summarize our findings in § 11.

The  $\Lambda$ CDM cosmological model is adopted, with  $\Omega_M = 0.3$ , and  $\Omega_\Lambda = 0.7$ , but with  $h$  left in units of  $H_0/100$  km s $^{-1}$  Mpc $^{-1}$ , for easier comparison with earlier work.

## 2 SUBARU DATA REDUCTION

We analyze deep images of three intermediate-redshift clusters, A1703 ( $z = 0.258$ ), A370 ( $z = 0.375$ ) and RXJ1347-11 ( $z = 0.451$ ), observed with the wide-field camera Suprime-Cam (Miyazaki et al. 2002) in several optical bands, at the prime focus of the 8.3m Subaru telescope. The cluster A1703 was observed on 2007 June 15 and the WL signal analyzed by Broadhurst et al. (2008) and Oguri et al. (2009). The observations of the other two clusters are available in the

**Table 1.** The Cluster Sample: Redshift and Filter Information

Cluster	$z$	$r_{vir}^1$ ( $h^{-1}$ Mpc)	Filters	Total exposure time (sec)	$m_{lim}^2$ (AB mag)	Seeing (arcsec)	Detection Band
A1689	0.183	1.9	$V_J$	1920	26.5	0.82	$i'$
			$i'$	2640	25.9	0.88	
A1703	0.258	1.7	$g'$	1200	27.4	0.89	$r'$
			$r'$	2100	26.9	0.78	
			$i'$	1200	26.1	0.8	
A370	0.375	2.1	$B_J$	7200	27.4	0.72	$R_C$
			$R_C$	8340	26.9	0.6	
			$z'$	14221	26.1	0.7	
RXJ1347-11	0.451	1.6	$V_J$	1800	26.5	0.7	$R_C$
			$R_C$	2880	26.7	0.76	
			$z'$	4860	25.5	0.6	

<sup>1</sup>based on Broadhurst et al. (2008)

<sup>2</sup>limiting magnitude for a  $3\sigma$  detection within a  $2''$  aperture

Subaru archive, SMOKA<sup>1</sup>. Subaru reduction software (SDFRED; Yagi et al. 2002; Ouchi et al. 2004) is used for flat-fielding, instrumental distortion correction, differential refraction, sky subtraction, and stacking. Photometric catalogs are created using SExtractor (Bertin & Arnouts 1996) in dual-image mode, for which we use our deepest band as the detection image. Since our work relies heavily on the colours of galaxies, we prefer using isophotal magnitudes. Astrometric correction is done with the SCAMP tool (Bertin 2006) using reference objects in the NOMAD catalog (Zacharias et al. 2004) and the SDSS DR6 (Adelman-McCarthy et al. 2008) where available. The clusters observation details are listed in Table 1.

Photometric zeropoints were calculated from associated standard star observations and also from independent well calibrated photometry, where available. In the case of A1703 and A370, no standard star observations were available, so zeropoints were derived independently in similar passbands by comparing to magnitudes of stars observed in SDSS fields (Oguri et al. 2009). Conversions from SDSS  $g, r$  bands to Subaru  $B, R_C$  bands were done using the relations given in Lupton (2005) for the SDSS. For RXJ1347-11, standard stars observed during the observation nights were used to derive photometric zeropoints in the  $B, R_C$  and  $z'$  bands. For the  $z'$ -band only three Standard stars were unsaturated in the Subaru image. To better constrain the  $z'$ -band, and as a consistency check for the  $B_J$  &  $R_C$ -bands, unsaturated stars were compared with the *HST*/ACS images of RXJ1347-11 in the  $F475W, F814W$  &  $F850LP$  filters, finding good consistency to within  $\pm 0.05$  mag.

### 3 SAMPLE SELECTION FROM THE COLOUR-COLOUR DIAGRAM

For each cluster we use Subaru observations in three broadbands, which differ in their choice of passbands between the clusters, though all observations are deep and taken in conditions of good seeing, representing some of the highest quality

imaging of any target by Subaru in terms of depth, resolution, and colour coverage. Using three bands in terms of two-colour space for object selection will help separate different populations and improve subsequent WL and light measurements of the cluster, as we now demonstrate.

#### 3.1 Cluster Members

For all three clusters we construct a CC diagram and first identify in this space where the cluster lies. We do this by calculating the mean distance of all objects from the cluster centre in a given CC cell, as shown in Fig. 1. This turns out to be a very clear way of finding the cluster as the mean radius is markedly lower in a well defined region of CC space for each cluster (region of bluer (darker) colours, the approximate boundary of which is marked in black). This small region clearly corresponds to an overdensity of galaxies in CC space comprising the red sequence of each cluster and a blue trail of later type cluster members (Fig. 2, dashed white curve). Of course, some background galaxies must also be expected in this region of CC space, and the proportion of these will be established in § 7 by looking at their WL signal – which should be consistent with zero in the case of no background contamination. In general, a positive signal will be expected at some level, in proportion to the fraction of lensed background galaxies occupying that same region of CC space as the cluster. Indeed, it is clear that the level of the tangential distortion seen in Fig. 6 is consistent with zero almost to the outskirts of each cluster radial span, and only rises to meet the background level at large radius where the proportion of cluster members is small compared with the background counts. In Fig. 1 (black curve), in Fig. 2 (dashed white curve) and in Fig. 3 (left panels, green points) we mark the boundaries of this region, selected relative to the red sequence in this CC space, and conservatively to safely encompass the region occupied by the cluster.

The above sample, which includes all cluster member galaxies, we term the “green” sample, as distinct from the well separated populations of red and bluer galaxies discussed below (Fig. 3, left panels). In defining this green sample we apply a magnitude limit of  $m \simeq 26.5$  in the

<sup>1</sup> <http://smoka.nao.ac.jp>.

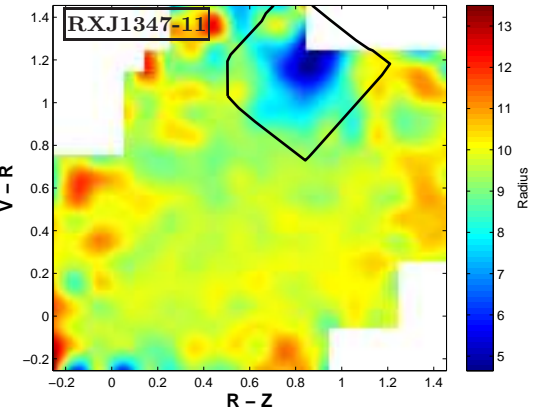
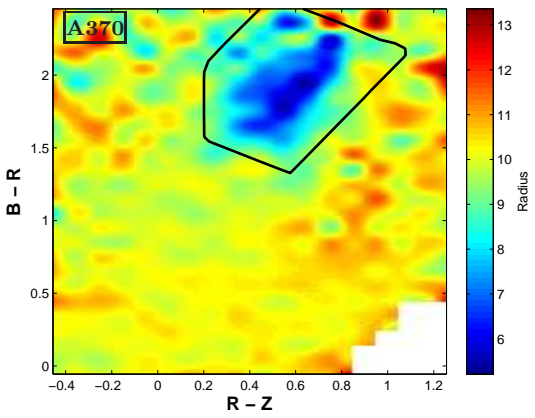
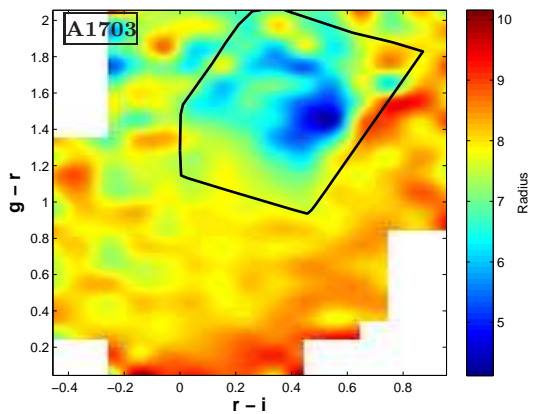


**Figure 1.** Averaged radius from cluster centre displayed in CC space for A1703, A370 & RXJ1347-11 (Top to bottom). The bluer (darker) colours imply average lower radius, hence correspond to the location of the cluster in CC space. The black box marks the boundaries of the green sample we select, which conservatively includes all cluster members.

reddest band available for each cluster ( $i'$ -band for A1703 and  $z'$ -band for A370 and RXJ1347-11), to which the data are complete for all three clusters. Beyond this limit incompleteness creeps into the bluer bands, complicating colour measurements, in particular of red galaxies. We also set a bright magnitude limit, according to the magnitude of the brightest cluster member in the same equivalent band.

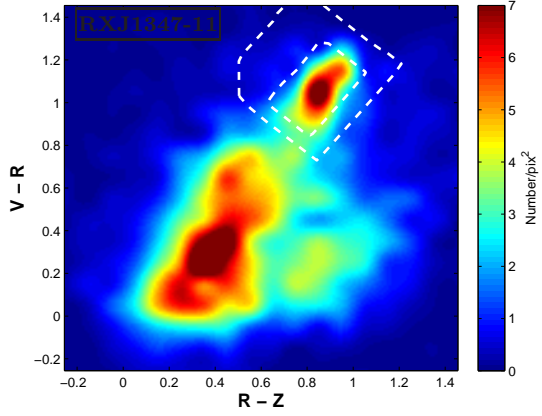
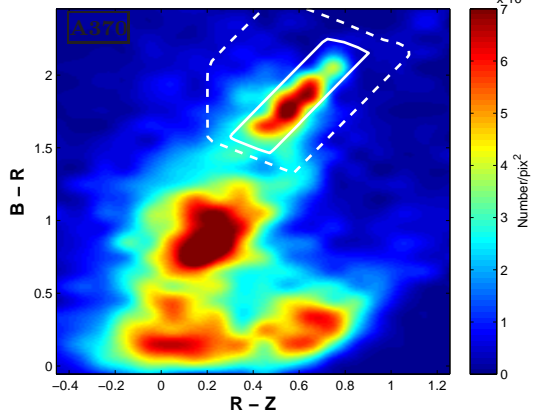
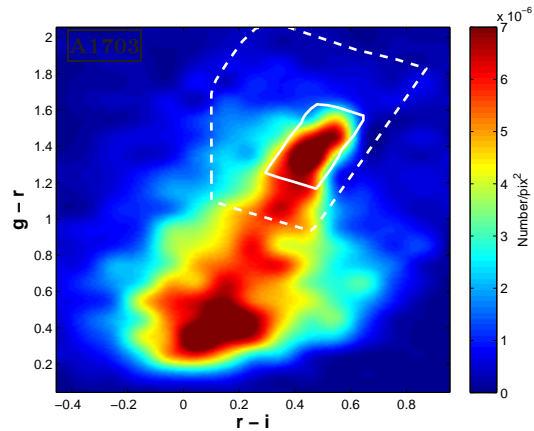


**Figure 2.** Number density in CC space for A1703, A370 & RXJ1347-11 (Top to bottom). The four distinct density peaks (seen especially in the A370 plot) are shown to be different galaxy populations - the reddest peak in the upper right corner of the plots (dashed white line) depicts the overdensity of cluster galaxies, whose colours are lying on the red sequence; the middle peak with colours bluer than the cluster shows the overdensity of foreground galaxies; the two peaks in the bottom part (bluest in  $B - R$ ) can be demonstrated to comprise of blue and red (left and right, respectively) background galaxies.

### 3.2 Red Background Galaxies

The mean radius used above is useful for locating the cluster in CC space but does not help in the definition of background or foreground galaxy populations, which are of course relatively uniform over the field of view, apart from the relatively small magnification bias which tends to deplete the number of red background galaxies towards the centre of mass, as described in Broadhurst et al. (2008) and is visible here in Fig. 3 (central panels, black squares) as a decrease in number counts towards the centre.

To define the foreground and background populations we look instead at the combination of the WL signal and the distribution of galaxies in the CC plane. For each cluster, we see a dense cloud of red objects (Fig. 2, lower right overdensity). This is particularly obvious for A370 where we have the widest wavelength coverage,  $B_J$ ,  $R_C$  &  $z'$ . The cloud is relatively red in  $R_C - z'$  but blue in  $B_J - R_C$ , so very well separated from the cluster member region defined above. This red cloud is known from wide-field survey work (Capak et al. 2007) and established to comprise early- to mid-type galaxies spanning a broad redshift range,  $0.5 < z < 2$ , as discussed below (§ 5).

For this red sample we define a conservative diagonal boundary relative to the red sequence as for the green sample (see Fig. 3, left panels, red points), to safely avoid contamination by cluster members and also foreground galaxies as discussed below (see § 3.3). We can check if there is any significant contamination of this red sample by unlensed galaxies by measuring the WL amplitude of these red galaxies as a function of distance from this boundary. As shown in Fig. 6 (red triangles), no evidence of dilution of the lensing signal is visible. We also define a blue colour limit to separate this red population from what appears to be a distinct density maximum of very blue objects – the so called “blue cloud” (see Fig. 2, in the extreme blue corner of CC space (see below § 3.3). We further limit the red sample to  $m < 26$  AB mag in the reddest band for each cluster to avoid incompleteness and so that we can rely on good detections in all bands when defining our colour samples.

The boundaries of the red sample as defined above are marked on Fig. 3 (red points), and can be seen to lie well away from the “green” cluster sample previously defined (green points). For this red sample a clearly rising WL signal is seen all the way to the smallest radius accessible ( $r \lesssim 1'$ ) for each cluster (Fig. 6, red triangles), with no sign of a central turnover which would indicate the presence of unlensed cluster members, as discussed fully in § 6.

### 3.3 Blue Background and Foreground Galaxies

Above we have been able to define the region of CC space occupied by cluster members by virtue of their clustered distribution. We have also defined with confidence a sample of red background galaxies lying well separated from cluster members and for which there is a clear WL signal. For bluer galaxies the situation is more complex as these may comprise blue cluster members, foreground objects and background blue galaxies. This is of particular concern where only one colour is available, and which we have shown in our earlier work can lead to a dilution of the WL signal of blue selected objects relative to the red background galaxies by unlensed

foreground galaxies and cluster members (Broadhurst et al. 2005; Medezinski et al. 2007).

We can see in the CC plane of each cluster that there are two regions lying blueward of the cluster within which most blue objects lie. For A370, where we have the deepest dataset, these density peaks are located around  $R_C - z' \sim 0$  and  $B_J - R_C \sim 0.8, 1.5$ . The redder of these two blue peaks lies in the centre of the CC plane, relatively close to the blue-end of the cluster sequence (see Fig. 3, left panels, magenta points). The spatial distribution of objects in this CC region shows no significant clustering about the cluster centre (see Fig. 3, middle panels, magenta circles). In addition, the WL signal of these objects (see Fig. 3, right panels, magenta circles) shows very little signal, indicating this is a predominately unlensed population, and together with the lack of clustering means this blue peak is dominated by galaxies lying in the foreground of the cluster. The lensing signal here is not strictly zero but marginally positive, implying a relatively low level of 10–20% lensed background galaxies. This region of CC space is clearly of no use for our purposes as it does not contain cluster members and is mostly unlensed. It is convenient, however, that the foreground unlensed population is so well defined in CC space as a clear overdensity and therefore can be readily excluded from our analysis. The redshift distribution of this population using deep field surveys (discussed in § 5) supports our finding that the bulk of this population lies at low redshift.

The bluer of the two peaks, in the extreme blue corner of CC space seen in Fig. 2 (lower left peak) is also unclustered on the sky, indicating no significant cluster members lie in this region (Fig. 3, middle panels, black squares). This blue overdensity is the well known “blue cloud” identified in deep field images. For each cluster, a clear WL signal is found for objects lying in this blue cloud (Fig. 6, blue circles), rising toward the centre of each cluster with a radial trend very similar to that of the red population ((Fig. 6, red triangles), indicating minimal foreground or cluster dilution of the WL signal. Objects lying in this region are expected to fall in the redshift range  $1 < z < 2.5$  (discussed below in § 5). Hence, we can safely conclude that these objects lie in the background with negligible cluster or foreground contamination, which would otherwise drag down the central WL signal. The boundaries we have chosen for this blue sample and plotted in Fig. 3 (left panels, blue points), are extended to include objects lying outside the main blue cloud but well away from the foreground and cluster populations defined above, in order to maximise the size of the blue sample but steering well clear of contamination by unlensed low redshift objects. We further limit the blue sample magnitude in the range  $22 < m_{AB} < 26$  to avoid contamination by very bright foreground galaxies, and to avoid incompleteness at the faint end.

## 4 EVOLUTIONARY COLOUR TRACKS

In order to examine in more detail the sample selection technique, we overlay evolutionary and empirical tracks on the CC plane, for different classes of galaxies. We first calculate non-evolving magnitudes in Subaru filters  $B_J$ ,  $R_C$ ,  $z'$  as a function of redshift using different galaxy templates constructed empirically for elliptical, Scd and starburst

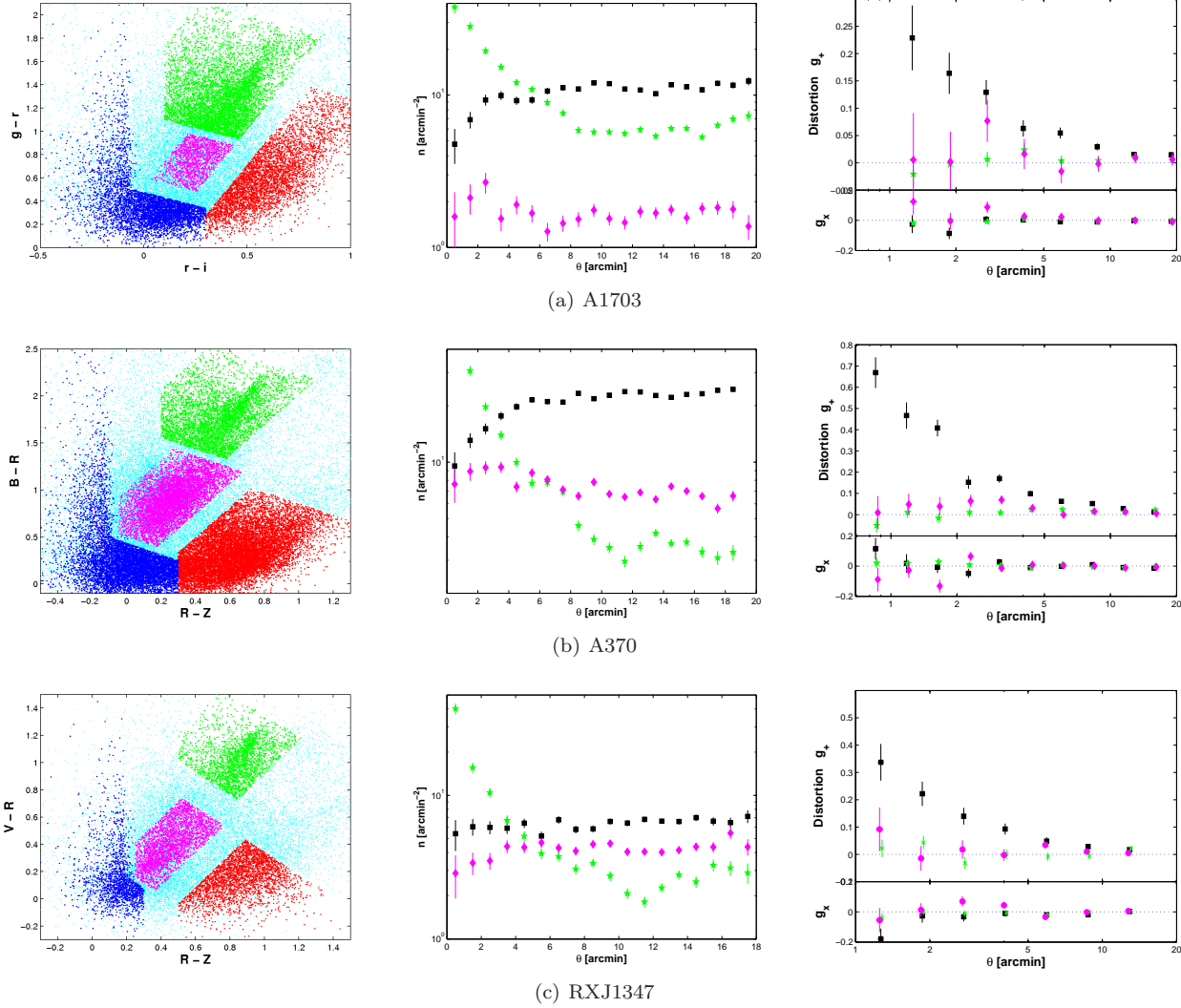


**Figure 3.** Sample selection and analysis. *Left:* CC diagrams, for A1703 (a), A370 (b) and RXJ1347-11 (c) (top to bottom), displaying the green sample, comprising mostly cluster member galaxies, and the red and blue samples, comprising of background galaxies. The galaxies that we identify as predominantly foreground lie in between the cluster and background galaxies are marked in magenta. *Centre:* Surface number density of galaxies vs. radius. Background (red+blue galaxies) density (black squares) is fairly constant with radius, except for a slight decrease in the central region (depletion due to lensing magnification effect). The green sample (green pentagrams) rises steeply toward the centre as expected for cluster members. The magenta sample (magenta diamonds) has a flat density profile, meaning these are not part of the cluster. *Right:* Tangential distortion vs. radius. The background (black squares) rises continuously toward the centre, representing real WL signal. The green sample distortion (green pentagrams) is essentially in agreement with zero, as expected from unlensed cluster galaxies, and the magenta sample distortion (magenta diamonds) is significantly lower than the background WL signal, indicating object selected in this CC range are mostly unlensed foreground galaxies. However, the magenta sample also contains to some extent background galaxies, therefore the WL signal is slightly higher than zero.

types from the Kinney-Calzetti library (Calzetti, Kinney & Storchi-Bergmann 1994; Kinney et al. 1996). The resulting colour tracks are overplotted in Fig. 4 (top) on the  $B_J - R_C$  vs.  $R_C - z'$  plane of A370. These templates show how the foreground population of galaxies in the centre of the CC plane quickly jumps above a redshift of  $\sim 1$  to the lower blue density peak. For the E/S0 it appears that even the no-evolution track is a good fit to a distribution of red galaxies which fall on a well-defined loop visible in the CC plane with a maximum red colour of  $B_J - R_C = 2.5$ ,  $R_C - z' = 1.5$  at a redshift of  $z \sim 0.8$ . The remainder of the loop is not well

constrained (and we therefore leave it out), likely where evolution kicks in making the SED of early-type objects bluer.

To generate evolving tracks representing the evolution of galaxy SED's, the Galev<sup>2</sup> (Kotulla et al. 2009) code was used to represent galaxy types with different star-formation histories – a short 3 Gyr starburst ( $Z_\odot$ ), E-type (exponentially declining SFR with  $Z_\odot$ ), S0 (gas-related SFR with  $Z_\odot$ ), Sa (gas-related SFR with  $2.5Z_\odot$ ), Sb (gas-related SFR with  $0.4Z_\odot$ ) and Sd (constant SFR with  $0.2Z_\odot$ ) (Fig. 4, bottom). It is evident that at low redshifts the modeled galaxies

<sup>2</sup> <http://www.galev.org/>

coincide with the high central peak we recognized above with our WL technique to be foreground, and as they are redshifted the colours of E/S0 galaxies agree at  $z \sim 0.4$  with the cluster colours. At higher redshifts the early types objects become bluer due to the effect of evolution, and also the late-type galaxies jump quickly across the valley and fall close to the observed trail of red and blue background galaxies at  $1 < z < 2$ . At even higher redshifts ( $z > 2.5$ ), they fade out from the  $B_J$ -band and become redder in  $B_J - R_C$ , agreeing with observed colours of dropout galaxies. Accounting for evolution, the tracks follow more carefully the trend around the lower-left blue corner ( $B_J - R_C \sim 0.1$ ,  $R_C - z' \sim 0$ ), seen clearly from the galaxy colour distribution.

In general, similar behaviour is seen for both methods, giving compelling evidence that in this CC plane the foreground and cluster galaxies are rather well-separated from the higher-redshift background galaxies, and support the picture we presented above for the safe selection of background galaxies for a WL study. The slight differences in colour (offset seen from the Galev models to bluer  $B_J - R_C$  colours for example) is interesting and may arise from the inclusion of evolution, the presence of dust or minor model uncertainties. The shape of the early-type galaxy loop is certainly worth exploring in greater detail and may help to constrain the general evolutionary history of early-type galaxies.

## 5 DEPTH ESTIMATION FROM SDF/COSMOS

The lensing signal is dependent on the source distance, scaling linearly with  $D_{ls}/D_s$ , the lensing distance ratio. We thus need to estimate and correct for the respective depths of the different samples. To this end we rely on accurate photometric redshifts derived for two deep, multi-band field surveys, the Subaru Deep Field (SDF; Kashikawa et al. 2004), and COSMOS (Capak et al. 2007). For the SDF, photometric redshifts are calculated with BPZ (Benítez 2000), using a new template library, generated using a set of PEGASE templates (Fioc & Rocca-Volmerange 1997) which approximates the library described in Benítez et al. (2004) and Coe et al. (2006). This new library has an accuracy of  $\delta z/(1+z) = 0.037$  with the FIREWORKS catalog (Wuyts et al. 2009) and a low catastrophic error rate. Using those photo- $z$ , and the spectral classification provided by BPZ, we generate magnitudes in the required Subaru filters to match the cluster observations. We select samples according to CC/magnitude limits described above (Fig. 3) for A370 and RXJ1347-11 (the SDF filters are not matched with the filters used for A1703). The resulting redshift distributions of the green (thin solid line), red (thick solid line), blue (dashed line) and foreground (dash-dotted line) samples selected to match A370 samples using SDF are displayed in Fig. 5 (top).

For COSMOS, photometric redshifts have been derived by Ilbert et al. (2009) using 30 bands in the UV to mid-IR. Since the COSMOS photometry does not cover the Subaru  $R_C$  band, we need to estimate  $R_C$ -band magnitudes for it. We use the HyperZ (Bolzonella, Miralles & Pelló 2000) template fitting code to obtain the best-fitting spectral template for each galaxy, from which the  $R_C$  magnitude is derived with the transmission curve of the Subaru  $R_C$ -band filter (see Umetsu et al. 2009b). We then select samples by ap-

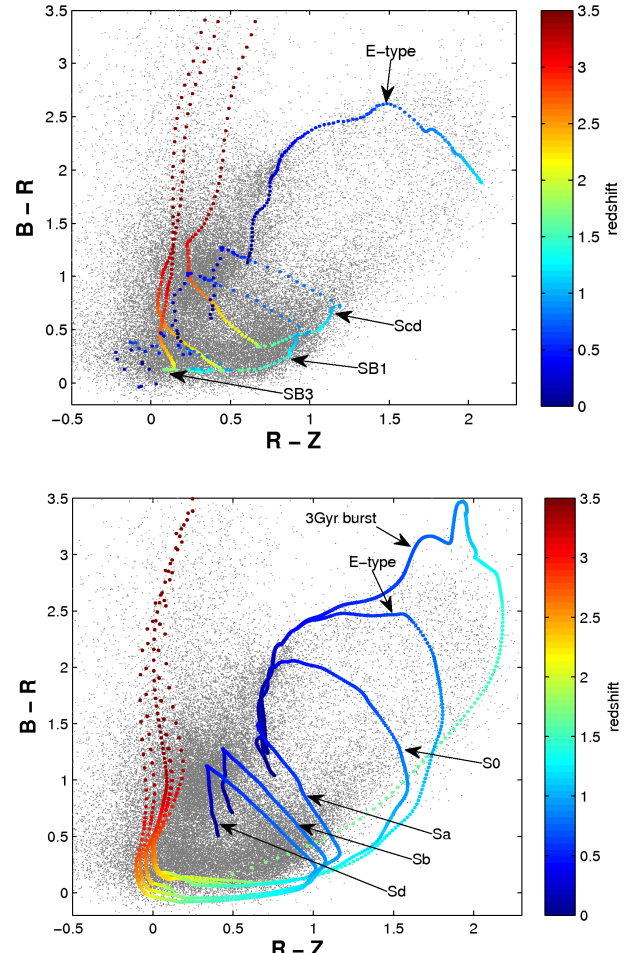


**Figure 4.** Top: Empirical colour tracks overlaid on the galaxy distribution of A370 in  $B_J - R_C$  vs.  $R_C - z'$  plane, for a range of galaxy templates: elliptical, Scd, SB1 and SB3 SED's. Bottom: Synthetic colour tracks including evolution, calculated with the Galev code for a single 3 Gyr burst, elliptical, S0, Sa, Sb and Sd type models.

plying the same CC/magnitude limits as for A1703, A370 and RXJ1347-11. The resulting redshift distributions of the green (thin solid line), red (thick solid line), blue (dashed line) and foreground (dash-dotted line), samples selected to match A370 samples using COSMOS are displayed in Fig. 5 (bottom). The results for each sample using SDF or COSMOS are summarized in table 2.

Although SDF is deeper, COSMOS redshifts are based on more bands over a wider spectral range. However, as stated in Ilbert et al. (2009), COSMOS photo- $z$ 's are reliable only to a magnitude of  $i' < 25$ , which is below our magnitude cutoff for the sample selection. We therefore make sure to limit our redshift estimation for the green sample to  $z < 3$ , to avoid mistakenly including high- $z$  dropouts that lie above the cluster in CC due to slight photometric offsets or unreliable photo- $z$ 's. Note we are only interested in the mean  $D_{ls}/D_s$  of **background** objects, and therefore estimate the depth of background galaxies present in the green sample in the range  $z_{cluster} < z < 3$ . Overall, the redshift distributions of both field surveys look quite similar, and there is

**Table 2.** CC-selected Sample Properties

Cluster	Sample	magnitude limits	N	$\bar{n}$ arcmin $^{-2}$	$\bar{z}_s$ COSMOS SDF	$\langle D_{ls}/D_s \rangle$ COSMOS SDF
A1703	green	$16.3 < i' < 26.5$	5678	6.2	0.54 -	0.45 -
	red	$21 < i' < 26$	4742	5.2	1.00 -	0.67 -
	blue	$22 < i' < 26$	4467	4.9	1.59 -	0.74 -
A370	green	$16.5 < z' < 26.5$	5369	5.3	0.46 0.69	0.25 0.29
	red	$21 < z' < 26$	13372	13.7	1.14 1.21	0.57 0.57
	blue	$22 < z' < 26$	8481	8.7	1.74 1.65	0.64 0.56
RXJ1347-11	green	$17.5 < z' < 26.5$	2512	3.5	0.67 0.79	0.28 0.31
	red	$21 < z' < 26$	2943	4.1	1.09 1.26	0.49 0.52
	blue	$22 < z' < 26$	1691	2.3	1.45 1.67	0.44 0.46

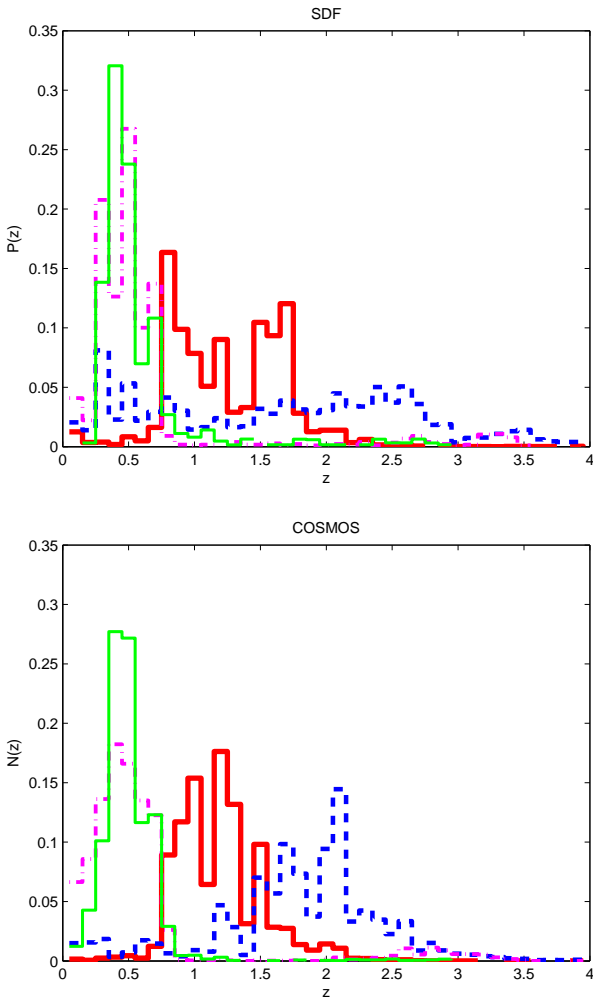


**Figure 5.** Redshift distributions of CC-selected samples. Two deep field surveys are used to estimate mean redshifts and depth: SDF (top), and COSMOS (bottom). The green (green thin solid line), red (red thick solid line), blue (blue thick dashed line) and foreground (magenta dotted-dashed line) samples are selected according to A370 CC/magnitude limits (see Fig. 3).

good agreement between values derived with either SDF or COSMOS, to  $\sim 10\%$  level in the depth, which can be due to the differences mentioned above. These depth values will be used later to correct the lensing signal (see § 7).

Importantly, this redshift analysis independently supports our assessment in both sections 3 & 4 that the various regions of the CC space correspond to differing populations. In particular the foreground population isolated in the centre of the CC diagram (shown in Fig. 3, magenta points, whose redshift distribution is shown in Fig. 5, magenta dotted-dashed curve) corresponds to predominantly low redshift galaxies  $\bar{z} \simeq 0.4$ , most of which are in the foreground of the clusters examined here, or at such low redshift behind the cluster that the lensing signal is small by virtue of the small separation,  $D_{ls}$ , between the lens and the source. In contrast, the red and blue populations are much more distant lying well behind our clusters, supporting our conclusion that the continuously rising WL signal of these populations is not significantly contaminated by cluster members. This also indicates that the predicted level of unlensed foreground galaxies is negligible for the red sample, as expected, and with only a possible  $\sim 10\%$  dilution in the blue.

## 6 WEAK LENSING ANALYSIS

We use the IMCAT package developed by N. Kaiser<sup>3</sup> to perform object detection and shape measurements, following the formalism outlined in Kaiser, Squires & Broadhurst (1995, hereafter KSB). Our analysis pipeline is described in Umetsu et al. (2009b). We have tested our shape measurement and object selection pipeline using STEP (Heymans et al. 2006) data of mock ground-based observations (see Umetsu et al. 2009b, § 3.2). Full details of the methods are presented in Umetsu & Broadhurst (2008), Umetsu et al. (2009a) and Umetsu et al. (2009a). In short, we find that we can recover the weak lensing signal with good precision, typically,  $m \sim 5\%$  of the shear calibration bias, and  $c \sim 10^{-3}$  of the residual shear offset which is about one-order of magnitude smaller than the weak-lensing signal in the cluster

<sup>3</sup> <http://www.ifa.hawaii.edu/~kaiser/imcat>

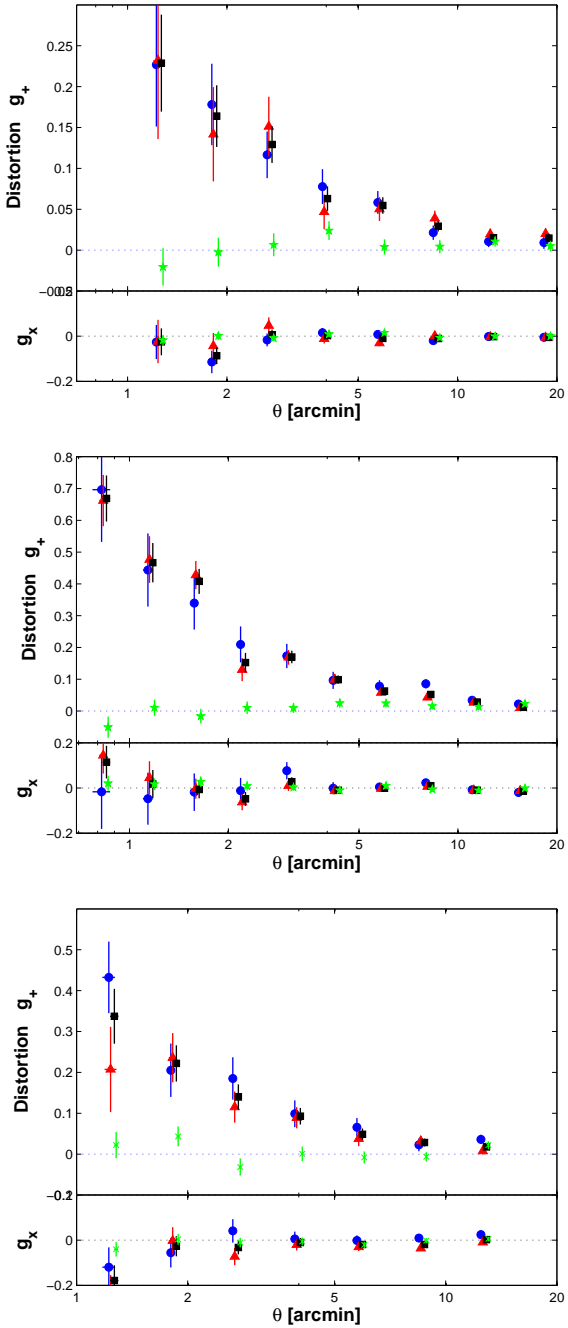


**Figure 6.** Tangential reduced shear vs. radius for A1703, A370 and RXJ1347-11 (top to bottom). The lower panels show the 45°-rotated ( $g_x$ ) component of the reduced shear. The green pentagrams represent the green sample, containing mostly cluster and some background galaxies whose colours are similar to the cluster. The black squares show the level of tangential distortion of the combined red+blue (triangles and circles, respectively) samples of the background. The green pentagrams slightly rise to the background level at large radii, indicating the green sample still contains some level of background galaxies at the outskirts of the cluster, and is consistent with zero towards the cluster centre where cluster members dominate the green sample and dilute the lensing signal.

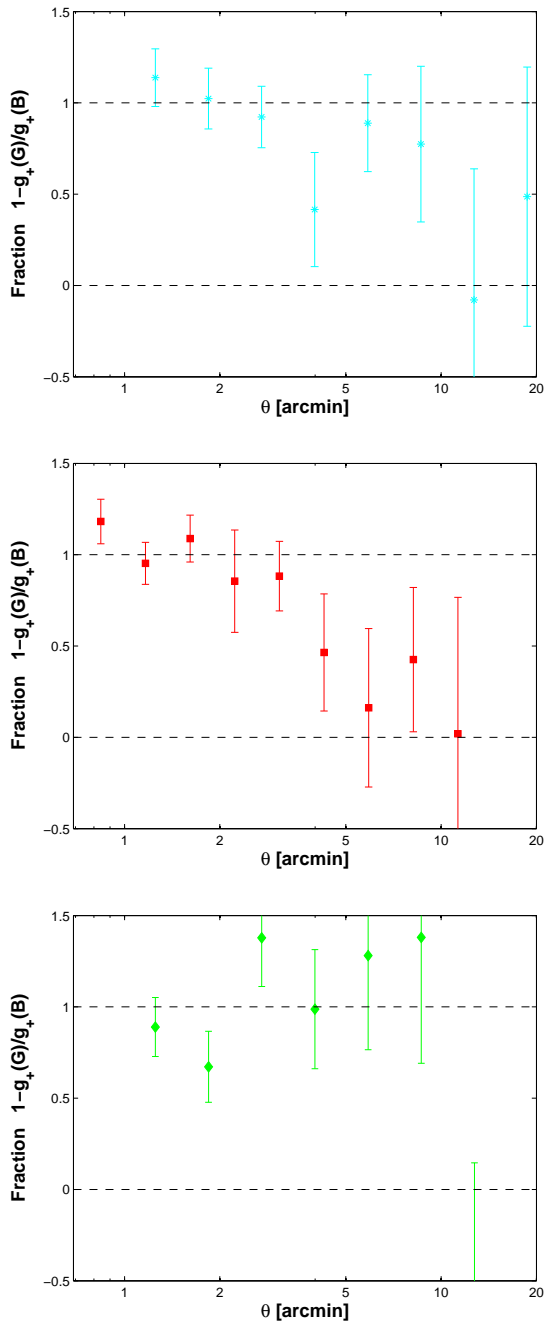


**Figure 7.** Fraction of cluster membership vs. radius for A1703, A370 and RXJ1347-11 (top to bottom). Cluster membership is proportional to the dilution of the distortion signal of the green sample, relative to the expected distortion of the background galaxies set by the combined red and blue samples. The fraction departs from unity only at large radius.

outskirts ( $|g| \sim 10^{-2}$ ). We emphasize that this level of calibration bias is sub-dominant compared to the statistical uncertainty ( $\sim 15\%$ ) in the mass due to the intrinsic scatter in galaxy shapes. Rather, the most critical source of systematic uncertainty in cluster weak lensing is dilution of the distortion signal due to the inclusion of unlensed foreground and cluster member galaxies, which can lead to an underestimation of the true signal for  $R < 400$  kpc/h by a factor of

2–5, as demonstrated in Broadhurst et al. (2005), Medezinski et al. (2007) and here.

The shape distortion of an object is described by the complex reduced-shear,  $g = g_1 + ig_2$ , where the reduced-shear is defined as:

$$g_\alpha \equiv \gamma_\alpha / (1 - \kappa). \quad (1)$$

The tangential component of the reduced-shear,  $g_T$ , is used to obtain the azimuthally averaged distortion due to lensing, and computed from the distortion coefficients  $g_1, g_2$ :

$$g_T = -(g_1 \cos 2\theta + g_2 \sin 2\theta), \quad (2)$$

where  $\theta$  is the position angle of an object with respect to the cluster centre, and the uncertainty in the  $g_T$  measurement is  $\sigma_T = \sigma_g / \sqrt{2} \equiv \sigma$  in terms of the RMS error  $\sigma_g$  for the complex reduced-shear measurement. To improve the statistical significance of the distortion measurement, we calculate the weighted average of  $g_T$  and its weighted error, as

$$\langle g_T(\theta_n) \rangle = \frac{\sum_i u_{g,i} g_{+,i}}{\sum_i u_{g,i}}, \quad (3)$$

$$\sigma_T(\theta_n) = \sqrt{\frac{\sum_i u_{g,i}^2 \sigma_i^2}{(\sum_i u_{g,i})^2}}, \quad (4)$$

where the index  $i$  runs over all of the objects located within the  $n$ th annulus with a median radius of  $\theta_n$ , and  $u_{g,i}$  is the inverse variance weight for  $i$ th object,  $u_{g,i} = 1/(\sigma_{g,i}^2 + \alpha^2)$ , softened with  $\alpha$ . We choose  $\alpha = 0.4$ , which is a typical value of the mean RMS  $\bar{\sigma}_g$  over the background sample. The case with  $\alpha = 0$  corresponds to an inverse-variance weighting. On the other hand, the limit  $\alpha \gg \sigma_{g,i}$  yields a uniform weighting. We have confirmed that our results are insensitive to the choice of  $\alpha$  (i.e., inverse-variance or uniform weighting) with the adopted smoothing parameters.

In Fig. 6 we plot the radial profile of  $g_T$  of the green (pentagrams), red (triangles) and blue (circles) samples defined above. The black squares represent the red+blue combined sample, showing the best estimate of the lensing signal. The red and blue samples profiles rise continuously toward the centre for each of the clusters, and are in good agreement with each other, demonstrating that both are dominated by background galaxies and are not contaminated by the cluster at all radii. The  $g_T$  profile of the green sample lies close to zero, especially at small radii, but shows a small positive signal at large radius, close in amplitude to the background signal measured above, meaning at beyond  $\sim 5'$  there are few cluster members in comparison to “green” background galaxies. Indeed, the virial radius derived from our best fitting NFW model lies at about  $10' - 15'$  and so physically it is reasonable that the cluster population is small here. The measured zero level of tangential distortion interior to this radius for the green sample reinforces our CC selection.

## 7 WEAK LENSING DILUTION

We can now estimate the fraction of cluster galaxies by taking the ratio of the WL signal between the green sample and the background sample, with the background including both red and blue galaxies as explained in § 3.

For a given radial bin ( $r_n$ ) containing objects in the

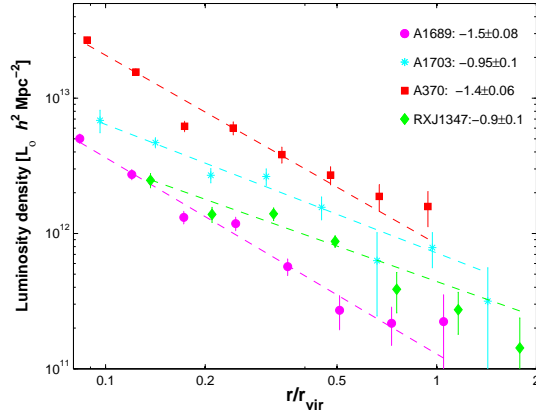


**Figure 8.** “g-Weighted” luminosity density vs.  $r/r_{vir}$  for A1689 (magenta circles), A1703 (cyan asterisks), A370 (red squares) and RXJ1347-11 (green diamonds). The flux  $F_i$  (green sample) of each galaxy is weighted by its tangential distortion  $g_{T,i}$  with respect to the background distortion signal. The dashed lines are the best fitting lines whose slopes are given in the legend. For clarity, the luminosity profiles have been shifted by a factor: A1703 shifted up by a factor of 2, A370 by a factor of 3, and RXJ1347-11 by a factor of 1.2.

green sample (§ 2), the mean value of  $g_T^{(G)}$  (eq. 3) is an average of the signal over cluster members and some background galaxies. Thus, its mean value  $\langle g_T^{(G)} \rangle$  will be lower than the true background level denoted by  $\langle g_T^{(B)} \rangle$  (Fig. 6) in proportion to the fraction of unlensed galaxies in the bin that lie in the cluster (rather than in the background), since the cluster members on average will add no net tangential signal. Therefore,

$$f_{cl}(r_n) \equiv \frac{N_{cl}}{N_{Green}} = 1 - \frac{\langle g_T(r_n)^{(G)} \rangle \langle D^{(B)} \rangle}{\langle g_T(r_n)^{(B)} \rangle \langle D^{(G)} \rangle} \quad (5)$$

is the cluster membership fraction of the green sample, where  $\langle D^{(B)} \rangle$  and  $\langle D^{(G)} \rangle$  are the mean lensing depths,  $D_{ls}/D_s$ , of the background and green galaxy samples, respectively, derived in § 5 (see full derivation in the appendix of Medezinski et al. 2007).

In Fig. 7 we show this ratio for each of our new clusters. In our previous analysis of A1689, where only colour-magnitude selection was done, many background galaxies were present in the green sample, so that only in the first radial bins the fraction of cluster galaxies was high, and gradually declined with radius (due to increasing fraction of background galaxies) at larger radii. Here, since we select a tight region around the cluster in CC and are able to better resolve it, our results show that the fraction is close to unity throughout the radial range of the cluster. Only in the outer bins, usually at  $r > 5' - 10'$  does the fraction decline, and we see a smaller percentage of cluster members. Large errorbars are introduced at outer radii since there are few cluster galaxies present, making it harder to use this effect in order to determine cluster membership.

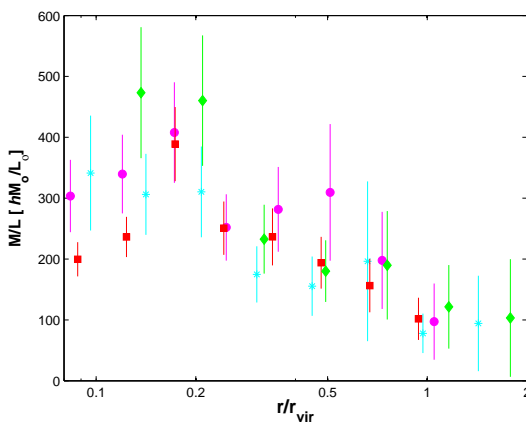


**Figure 9.** Mass-to-light ratio vs.  $r/r_{vir}$  for A1689 (magenta circles), A1703 (cyan asterisks), A370 (red squares) and RXJ1347-11 (green diamonds). The profiles are similar to each other, peaking around  $0.2r_{vir}$ , and declining continuously to the virial radius, which seems to be a general property of all well-studied clusters.

## 8 CLUSTER LIGHT PROFILES

We now turn to translate the deduced profile of membership fraction to a cluster luminosity profile. To account for the background contribution in the green sample and deduce only the cluster luminosity, we first measure the flux of all the galaxies in the green sample,  $\sum_i F_i^{(G)}$ , and then subtract the flux of the  $i$ -th galaxy weighted by its tangential distortion,  $g_i$ , relative to the background sample distortion,  $\langle g_T(r_n)^{(B)} \rangle$ . When averaged over the entire green sample this will have zero contribution from the unlensed cluster members, but will remove the contribution of background galaxies present in the green sample. The total flux of the cluster in the  $n^{\text{th}}$  radial bin is therefore,

$$F_{cl}(r_n) = \sum_i F_i^{(G)} - \frac{\langle D^{(B)} \rangle / \langle D^{(G)} \rangle}{\langle g_T(r_n)^{(B)} \rangle} \sum_i F_i^{(G)} g_{T,i}^{(G)} \quad (6)$$

and the flux is then translated to luminosity. First we calculate the absolute magnitude,

$$M = m - 5 \log d_L - K(z) + 5, \quad (7)$$

where the  $K$ -correction is evaluated for each radial bin according to its colour. The luminosity is simply,

$$L = 10^{0.4(M_\odot - M)} L_\odot, \quad (8)$$

where  $M_\odot$  is the absolute magnitude of the Sun (AB system) in the relevant band.

The results for all four clusters, including A1689, are shown in Fig. 8. As explained in § 3, the green sample comprises mostly of cluster galaxies, therefore the correction is not big for  $r < 10'$ , and only present at large radii, increasing the error. The cluster luminosity profiles mostly have a steady linear decline with radius, and are well described by a power-law fit, but with different slopes of  $d \log(L)/d \log(r) \sim -0.95 \pm 0.1, -1.4 \pm 0.06, -0.9 \pm 0.1$  for A1703, A370 and RXJ1347-11, respectively.

## 9 M/L PROFILES

We may now derive a radial profile of the differential mass-to-light ratio (often referred to as  $\delta M(r)/\delta L(r)$ ) by dividing the best-fit NFW projected mass density profile by the newly derived luminosity density profile obtained in § 8. The four  $M/L$  profiles are shown together in Fig. 9 to the limit of our data,  $\sim 3$  Mpc/h. The mass profiles for these clusters and their NFW fits were derived in our earlier work, Broadhurst et al. (2005) for A1689 and in Broadhurst et al. (2008) for A370, A1703 and RXJ1347 based on the sample selection scheme described in this paper.

For A1689, we found previously that the  $M/L$  ratio peaks at intermediate radius around  $r \sim 100h^{-1}$  kpc and then falls off to larger radius. Here we find a similar behavior for the other clusters, especially evident for A370, where  $M/L$  peaks at about  $r \sim 350h^{-1}$  kpc with values of  $M/L_R \sim 300 - 400 h(M/L)_\odot$ , and declines to values of  $M/L_R \sim 100 h(M/L)_\odot$  at the outskirts. A decline in  $M/L$  is also seen towards the centre of the cluster, reaching  $M/L_R \sim 200 h(M/L)_\odot$  below  $r \lesssim 200h^{-1}$  kpc. The  $M/L$  profile of A1703 also shows a similar trend, where it peaks at a radius of  $r \sim 200 - 300h^{-1}$  kpc with values of  $M/L_R \sim 300 h(M/L)_\odot$  and declines gradually to values of  $M/L_R \sim 100 h(M/L)_\odot$  at large radii. The profile of RXJ1347-11 declines from values of  $M/L_R \sim 400 - 500 h(M/L)_\odot$  at  $r \sim 200 - 300h^{-1}$  kpc to values of  $M/L_R \sim 100 h(M/L)_\odot$  at large radius.

The decrease in  $M/L$  values toward the centre of the cluster is only really evident for two clusters, A1689 and A370. For these clusters the luminosity profiles are relatively steep, and it is continuation of a steep power-law towards the centre that causes  $M/L$  to decline, as the mass profiles are not power-law but have a continuously declining gradient towards the cluster centres (NFW-like), so that the proportion of  $M/L$  declines markedly interior to the characteristic radius for these two clusters.

The decrease in  $M/L$  toward large radius seen for all four clusters is possibly explained by the increasing proportion of later type galaxies at larger radii, a manifestation of the morphology-density relation (Dressler 1980). Similar results have been shown by Rines et al. (2000) and Katgert et al. (2004); in Rines et al. (2000) where the differential  $M/L$  profile is similar to ours, with a decreasing  $M/L$  with radius, and their outermost value of  $M/L_R \sim 100 h(M/L)_\odot$  is in good agreement with the values we get for all our four clusters. Katgert et al. (2004) show a decrease at small radius, and by removing the brightest cluster members this decrease is shown to disappear.

The declining behavior is not simply accounted for by the change of stellar population with distance from the cluster centre. The galaxy colours show a very moderate decline with radius. In the case of A370, the radial colour gradient is  $d(B - z')/d \log(r) = -0.13 \pm 0.04$ , equivalent to a total change of  $\delta(B - z') = 0.12$  over the virial radius. This corresponds to a change in the mean stellar mass-to light ratio,  $M_*/L_R$ , of only  $\sim 17\%$ . Therefore, such a small correction alone cannot explain the declining trend of  $M/L$  with radius.

We now further examine the behaviour of  $M/L$  by separating cluster member galaxies by colour and by luminosity. There is a clear distinction between the  $M/L$  profiles based on colour selection as shown in Fig. 10. Tightly selecting just

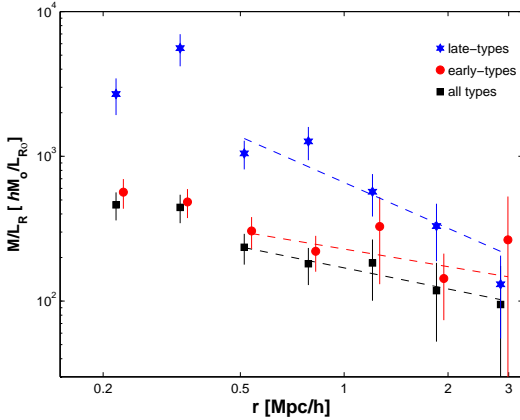
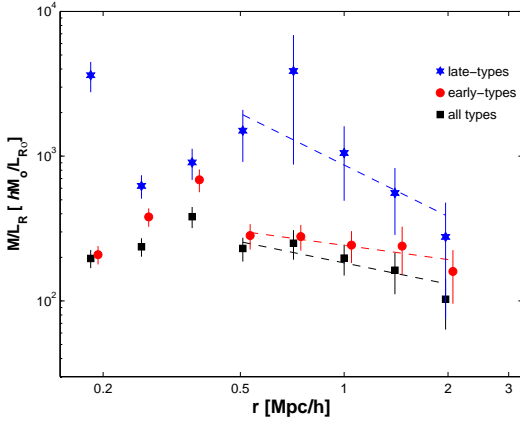
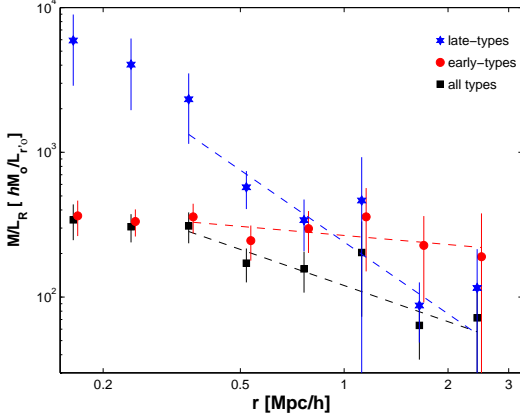


**Figure 10.** Mass-to-light ratio vs. radius for A1703, A370 and RXJ1347 (top to bottom plots) divided into two different cluster sub-populations. The black squares mark the entire green sample (same  $M/L$  profiles shown above in Fig. 9); the red circles mark a subsample from a tighter selection of cluster galaxies around the red sequence (white solid line marked in Fig. 2), mostly early-type elliptical galaxies. The blue hexagrams correspond to later-type cluster members (the rest of the green population inside the white dashed line, but outside the solid white line marked in Fig. 2). The slope of the declining outer profile is significantly steeper for the blue profiles, whereas for the red profiles the  $M/L$  is much flatter.

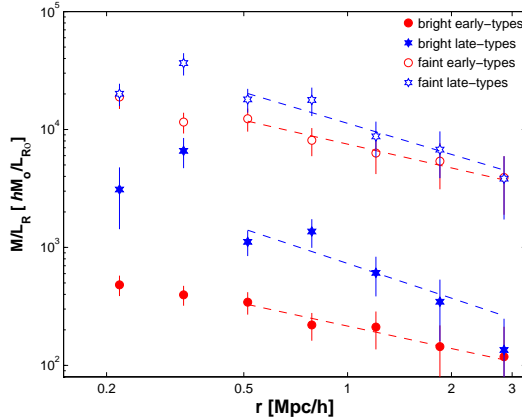
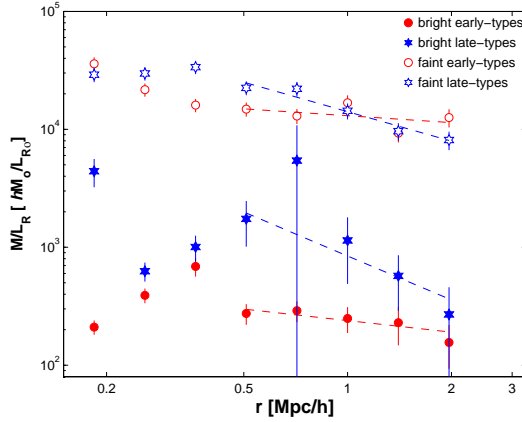
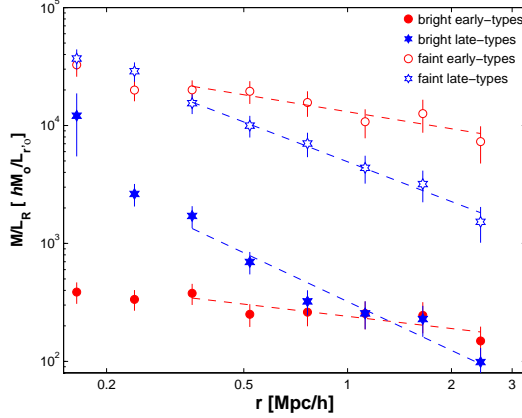


**Figure 11.** Mass-to-light ratio vs. radius for A1703, A370 and RXJ1347 (top to bottom plots) for early (red circles) and late type (blue hexagrams) clusters members, as in Fig. 10, but divided into high- (solid) and low-luminosity (empty) subsamples. Clearly the behavior of the early and later types is not a strong function of luminosity.

the sequence galaxies (inside the white solid line marked in Fig. 2) the  $M/L$  profiles are relatively flatter for all the clusters (Fig. 10, red circles), showing mild decline with radius, whereas the remaining non-sequence objects (the rest of the green population between the white dashed line and the solid white line marked in Fig. 2) have a steep dependence (Fig. 10, blue hexagrams) which is clearly responsible for the majority of the trend of  $M/L$  found above for the

cluster population as a whole (Fig. 10, black squares). If we now further divide these subsamples by luminosity into two broad bins as shown in Fig. 11, we see that this difference between the sequence and non-sequence populations is not strongly dependent on luminosity. If we also look at the number-density profile of each of these four subsamples (Fig. 12), we see that the early-type galaxies (red circles) are more concentrated than the later types (blue hexagrams), independently of luminosity.

It is evident from the above comparisons that later-type galaxies are relatively rare in the cluster centre, an effect which most likely has its origins in tidal and/or stripping of infalling later-type galaxies and their transformation into redder and rounder galaxies predominating in cluster centres. We now explore tidal effects in this context and comment on other related work.

### 9.1 Tidal and Ram-Pressure Stripping

In CDM-dominated cosmological models, the growth of structure is hierarchical, with clusters evolving through many merger events during which galaxies are dynamically affected to a varying degree based on their formation times and spatial locations in their parent systems. This process can be described by the excursion set formalism (Lacey & Cole 1993) with more detailed insight gained from hydrodynamical simulations. It has been clearly demonstrated that during these merger events DM haloes suffer pronounced tidal stripping (e.g., Moore et al. 1996). Detailed N-body simulations indicate that up to 70% of the mass may be stripped from halos orbiting close to the centre of massive clusters when integrated over the Hubble time, and with  $\sim 20\%$  loss even near the virial radius (Nagai & Kravtsov 2005). Statistical evidence for halo truncation is claimed also from lensing based measurements (Natarajan et al. 2002, 2009).

As can be expected, simulations show that despite the substantial effect of tidal forces in removing the outer DM from galaxy halos, the stellar content of early-type galaxies is only weakly affected by tidal interactions due to the centralised location of most stars within the DM halos (Nagai & Kravtsov 2005; Reed et al. 2005). Hence, the ratio of total mass to galaxy luminosity is predicted to be approximately independent of radius in this context. In detail, the above simulations show a mild radial decline of the ratio of the total mass density over the number density of DM halos,  $M/n$ , as shown in Fig. 13 (dashed curve). The relatively gentle declining trend in this ratio is the result of tidal forces (Nagai & Kravtsov 2005; Reed et al. 2005), which act over time to reduce the number of sub halos in the inner region as compared to the cluster outskirts.

This  $M/n$  ratio is a very useful prediction of the simulations which may be readily compared to our data. For each cluster we indeed find a gentle decline in the ratio of the total mass to the number of early type galaxies, the mean slope of which is in very good agreement with the prediction as shown in Fig. 13. The declining trend in this ratio is seen in the region  $0.1 - 1 r_{vir}$ , in good agreement with the prediction by Nagai & Kravtsov (2005).

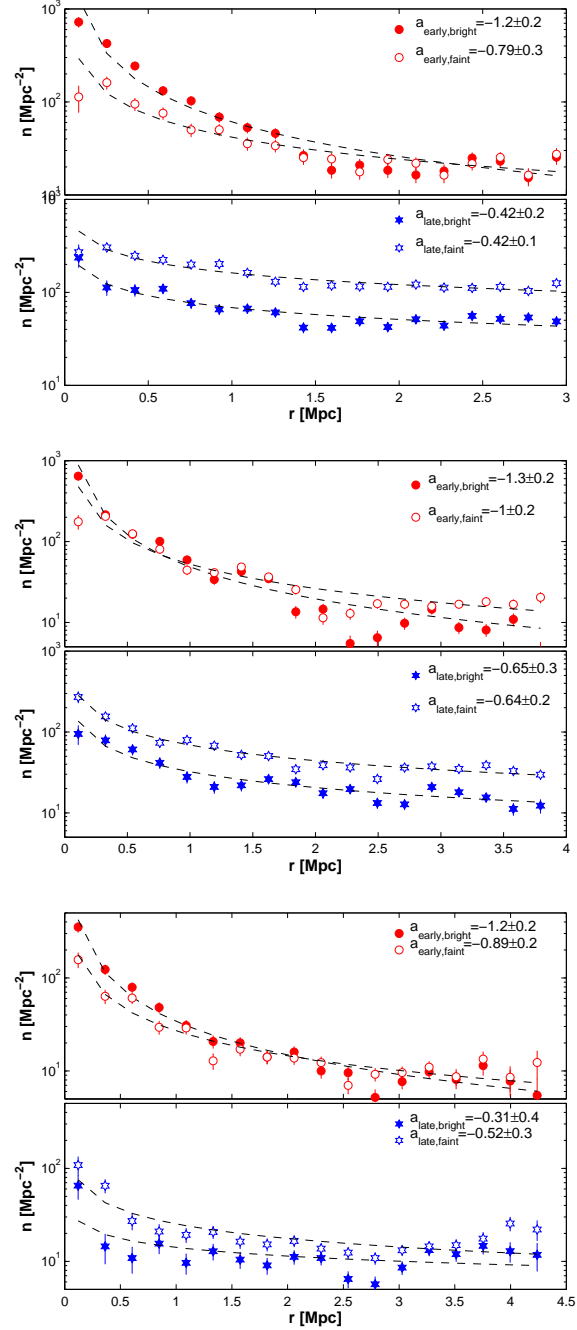


**Figure 12.** Number density profiles for A1703, A370 and RXJ1347-11 (top to bottom plots) for early (upper panels, red circles) and late (lower panels, blue hexagrams) type cluster members further divided into high (solid) and low-luminosity (empty) subsamples (as in Fig. 11). The redder profiles are more centrally concentrated than the bluer profiles, suggesting the proportion of early- to late-type members is a clear function of radius but not as much of luminosity, favouring early-types at smaller radius.

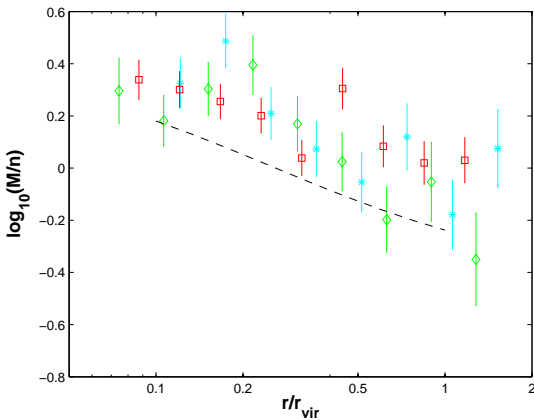


**Figure 13.** Radial profile of the ratio of the cluster mass density over the galaxy number density for A1703 (cyan stars), A370 (red squares) and RXJ1347-11 (green diamonds). Dashed line shows this ratio as calculated from the simulations of Nagai & Kravtsov (2005). The observed trend is similar to the theoretical prediction for each of the clusters and can be attributed theoretically to tidal effects by the cluster acting on the galaxy DM halos.

As we showed in § 9 the ratio of the total mass density to bluer cluster members light density has a very steep decline with radius – much greater than the mild trend observed above for early-type red sequence galaxies. The tendency towards an increasing proportion of early-type galaxies near cluster centres (also evident in Fig. 12) is of course well known and is understood empirically to result from the disruption of the gaseous disks of infalling galaxies. Radio continuum observations reveal that “wide-angle tails” of gaseous material appearing to trail behind disk galaxies (e.g., Marvel, Shukla & Rhee 1999). Recently spectacular large trails of  $H_\alpha$  emission have been detected around disk galaxies in the Coma and Virgo clusters (Bravo-Alfaro et al. 2000; Vollmer et al. 2004; Kenney et al. 2008). The most impressive object is a large spiral galaxy (NGC 4438) with obvious disrupted arms and a long trail ( $\sim 120$  kpc) of  $H_\alpha$  emission revealing the orbit of this galaxy has been bent around the massive central galaxy, M86, with a large relative velocity of  $\sim 500$  km/s (Kenney et al. 2008).

Ram-pressure stripping has long been calculated to be important (Gunn & Gott 1972) for disk galaxies (in clusters), removing preferentially the relatively low-density gas within a characteristic stripping radius, the scale of which can be estimated from basic considerations, and which was verified by careful simulations (Abadi, Moore & Bower 1999; Kronberger et al. 2008). The loss of gas has a transformative effect on both the morphology and the colours of such objects, a process which is claimed as a natural explanation for the cluster populations of S0 galaxies, (Homeier et al. 2005; Postman et al. 2005; Poggianti et al. 2009; Huertas-Company et al. 2009) and which is also related to the evolution of cluster gas metallicity (Schindler et al. 2005; Arieli, Rephaeli & Norman 2008).

## 10 CLUSTER LUMINOSITY FUNCTIONS

The data allow the LF to be usefully constructed in several independent radial and magnitude bins, and hence we can examine the form of the LF of cluster members as a function of projected distance from the cluster centre. By measuring the degree of dilution separately in each magnitude bin we can construct LFs without resorting to uncertain background subtraction.

Here, the dilution correction is evaluated as a function of magnitude and radius. Left panels of Fig. 14 show the tangential distortion of the green sample versus absolute magnitude bin, and the reference background distortion level is marked in the black solid line; see (Medezinski et al. 2007) for more details. To correct for this we apply equation (5) to each magnitude bin:

$$\Phi_{cl}(M_k) = \Phi(M_k)[1 - \langle g_T^{(G)}(M_k) \rangle / \langle g_T^{(B)}(r) \rangle] \quad (9)$$

(Note that the background signal is averaged over the whole range of magnitudes at that radius). The correction for background present in the green sample is in fact not large for the brighter bins, but is more essential at the fainter bins, with magnitude  $M_R \gtrsim -18$ . This is similar to the observation we made in § 7 for the radial profile of the fraction correction, only there the correction was a function of radius, and here it is a function of magnitude.

We construct LFs in three broad radial annuli, except for RXJ1347-11 for which this is feasible – due to its small angular size – only in two bins. The results are shown in Fig. 14 (centre panels). Each LF is well fitted by a Schechter (1976) function (dashed lines), and the confidence contours for the Schechter function parameters  $M_*$  and  $\alpha$  are shown on the right-hand panels of Fig. 14. The Schechter fit parameters are also specified in table 3. Clearly there is no evidence for a distinct upturn, to the limits of the photometry of any of our clusters. The slope of the Schechter function is well defined in each case, lying in a tight range, from  $\alpha = -0.95 \pm 0.05$  to  $\alpha = -1.24 \pm 0.2$ . Also, there is no significant radial dependence in the shape of the LFs with distance from the cluster centre. There may however be some evidence that in the outer radial bin the LFs are somewhat steeper than in the centre of the cluster for A1703, as can be seen in Fig. 14, where the slope changes from  $\alpha \sim -0.95$  to  $\alpha \sim -1.1$  to  $\alpha \sim -1.25$  at larger radius. The knee of the LFs, namely the bright-end break, is very distinct, and is around  $M_{*r'} \sim -21.5$  for A1703,  $M_{*R} \sim -22.5$  for A370, and  $M_{*R} \sim -22$  for RXJ1347-11.

For A1689 we also saw no upturn at the faint magnitude limit, with  $\alpha = -1.05 \pm 0.07$  (Medezinski et al. 2007). There has been some significant disagreement regarding the shapes and faint-end slopes of LFs in clusters. Popesso et al. (2006) analyzing 69 RASS-SDSS clusters found a steep upturn at the faint-end by fitting a composite of two Schechter functions, with the faint-end fit slope being  $\alpha \sim -2$ . Rines & Geller (2008) made a comprehensive study of two local galaxy clusters, using spectroscopic data to identify securely the cluster galaxies, for a more reliable measurement of cluster LFs. They found no distinct upturn for either of the clusters, with  $\alpha = -1.13$  for A2199 and  $\alpha = -1.28$  for the Virgo cluster. When measuring the overall slope of the composite cluster LF, i.e., up to the virial radius, we find slopes of  $\alpha \sim -1.1 \pm 0.1$  for all three clusters, in good agreement with

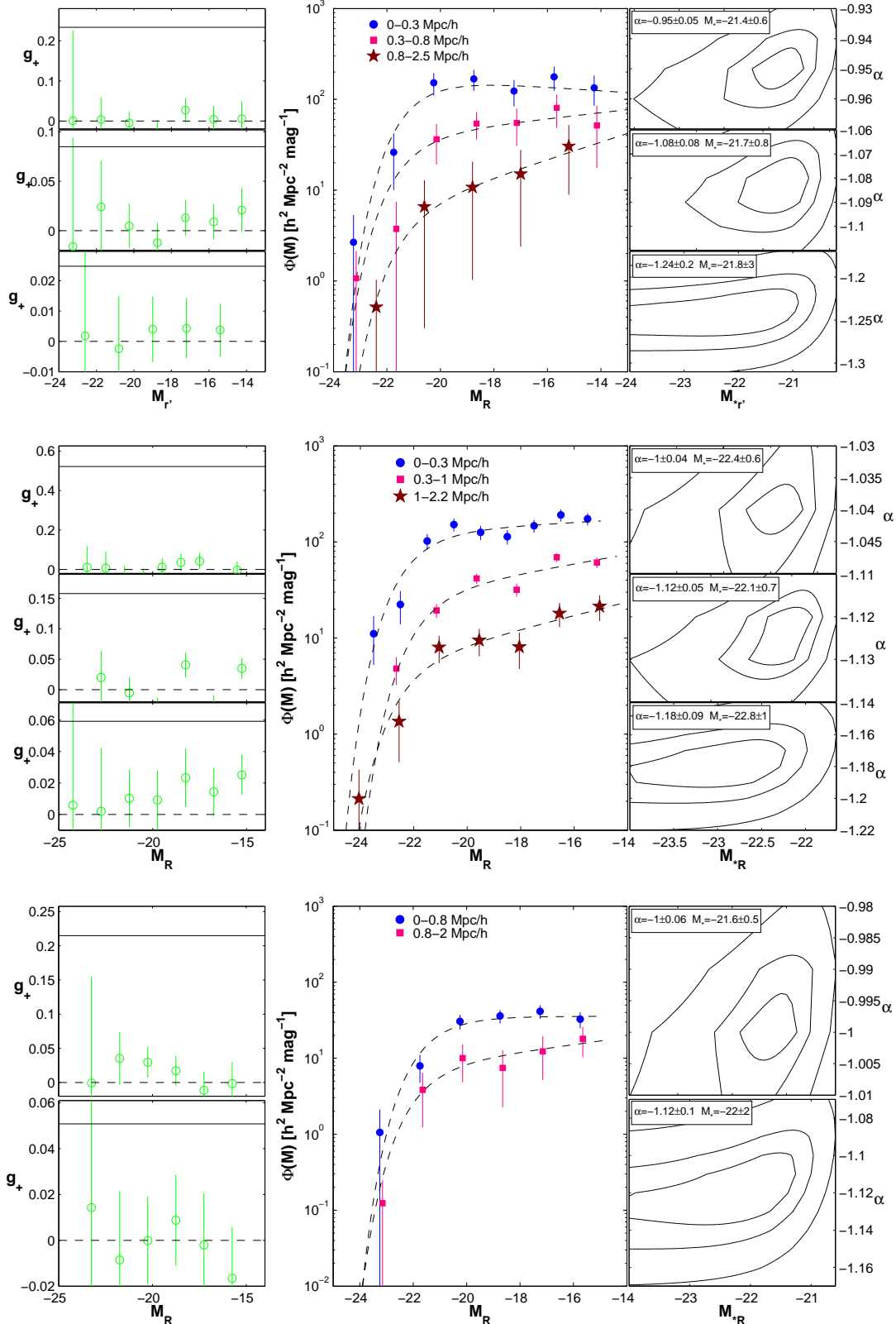


**Figure 14.** Luminosity functions of A1703 (top), A370 (middle) and RXJ1347-11 (bottom). Centre part: LFs and their Schechter fits are shown for several independent radial bins, indicating little trend of the shape of the LF with radius. Left part: tangential distortion  $g_T$  of the green sample as a function of magnitude used in the derivation of the corresponding LF. Right part: 1 $\sigma$ , 2 $\sigma$ , and 3 $\sigma$  contours for the Schechter function fits parameters  $M_*$  and  $\alpha$ , for each of the corresponding LFs of each radial bin.

**Table 3.** Parameters of Schechter fits to the Luminosity function

Cluster	radial range (Mpc/h)	$\alpha$	$M_*$
A1703	0 – 0.3	$-0.95 \pm 0.05$	$-21.4 \pm 0.6$
	0.3 – 0.8	$-1.08 \pm 0.08$	$-21.7 \pm 0.8$
	0.8 – 2.5	$-1.24 \pm 0.2$	$-21.8 \pm 3$
A370	0 – 0.3	$-1 \pm 0.04$	$-22.4 \pm 0.6$
	0.3 – 1	$-1.12 \pm 0.05$	$-22.1 \pm 0.7$
	1 – 2.2	$-1.18 \pm 0.09$	$-22.8 \pm 1$
RXJ1347-11	0 – 0.8	$-1 \pm 0.06$	$-21.6 \pm 0.5$
	0.8 – 2	$-1.12 \pm 0.1$	$-22 \pm 2$

the results of Rines & Geller (2008). We note that general cluster-to-cluster variation in the total LF fits is not necessarily unexpected, but probably depends on the specific characteristics of individual clusters. Our clusters all show relatively flat LFs, with only a weak radial dependence.

## 11 DISCUSSION AND CONCLUSIONS

In this paper we have compared in detail the dark and luminous properties of three high mass galaxy clusters, A1703, A370 and RXJ1347-11, and examined the relation between mass and light all the way out to the virial radius. We have further applied the WL dilution approach previously developed for A1689 (Medezinski et al. 2007) as an alternative means of obtaining the LF and light profiles of galaxy clusters. This based on the dilution of the lensing distortion signal by unlensed cluster members, and has the advantage of being independent of density fluctuations in the background.

We have examined clusters A1703, A370 and RXJ1347-11 for which data of exceptional quality has been taken with Subaru/Suprime-Cam in multiple passbands. We have shown how a careful separation of the cluster, foreground, and background galaxies can be achieved using weak lensing information galaxy colours. We also make use of the clustering of cluster members, finding the cluster members are confined to a distinct region of CC space with relatively small mean radial distances. We have constructed a reliable background sample for WL measurements, by selecting red background galaxies whose WL signal rises all the way to the centre of the cluster, and adding to those the faint cloud of very blue galaxies, whose WL signal we have shown is in good agreement with the red galaxies. We have avoided dilution of the WL signal by identifying and excluding the foreground population in the CC diagram for which no clustering or WL signal is detected. Together, the red and blue samples WL measurements can be used to reconstruct accurate mass maps of all four clusters (see Broadhurst et al. 2008).

By applying this sample selection and WL dilution correction, the LFs are derived for each of the clusters, in several radial bins, without the need of statistical background subtraction. The LFs extend to very faint magnitude limits,  $M_R \sim -14$ , and each shows a very flat faint-end slopes,  $-0.95 \leq \alpha \leq -1.24$ , in agreement with our previous study for A1689. There are various claims in the literature regarding the shape of the faint end of the galaxy LF (Popesso et al.

2006; Rines & Geller 2008; Adami et al. 2008; Crawford, Bershady & Hoessel 2009), with relatively flat slopes measured and found consistent with a simple Schechter function, and other work claiming a distinctive upturn at faint magnitudes. Differences may conceivably represent intrinsic differences between clusters, but a worry here is the uncertain subtraction of the steep background counts of faint galaxies when evaluating the background using control fields. Uncertainties may result from inherent clustering of the background galaxies and also variations in photometric incompleteness, or differential extinction between the cluster and control fields.

Redshift measurements may remove concerns about the background for complete surveys, but in practice spectroscopy can only reach interestingly faint limiting luminosities for fairly local clusters, requiring multiplexing capability over a wide-fields of view on large telescopes. Rines & Geller (2008) recently provided the tightest constraints from spectroscopy out to a sizable fraction of the virial radius, finding no significant upturn for the clusters studied. Confidence is gaining in the use of photometric redshifts, from careful deep multi-colour imaging, which in the work of Adami et al. (2008) a relatively steep LF is claimed for Coma, but flatter slopes are measured for a sample of intermediate-redshift clusters (Crawford et al. 2009). Clearly, it is essential that there is no significant confusion of background galaxies with cluster members or foreground, as is achieved with our approach.

The radial light profiles of these clusters are well characterized by a power-law slope of approximately  $d \log(L)/d \log(r) \simeq -1$  over all radii. These are compared with the mass profiles from WL to derive the radial profile of the  $M/L$  ratio, a quantity which has hitherto not been constrained in much detail, due to the difficulty of measuring mass profiles with sufficient precision and light profiles free of systematic effects. Interestingly, we find that all our clusters show a very similar radial trend of  $M/L$ , peaking in the range  $M/L_R \sim 500 h(M/L)_\odot$  at intermediate radius  $\simeq 0.15 R_{vir}$ , and declining to approximately a limiting level of  $M/L_R \sim 100 h(M/L)_\odot$  toward the virial radius of each cluster.

The decline of  $M/L$  towards large radius is very interesting and seems to be a universal feature of clusters, or at least it is clearly found in the clusters we have been able to study here in sufficient detail and for A1689 (Medezinski et al. 2007). Additionally, in the careful dynamical-based study of Rines et al. (2000) a similar declining trend was found for A576. We have shown that such behavior is not simply accounted for by the change in the stellar content of galaxies with distance from the cluster centre. The radial trend of galaxy colours found is very mild and when corrected for using standard stellar population synthesis falls well short of explaining the marked trend of  $M/L$  with radius.

The variation of  $M/L$  is however seen to be almost entirely stemming from the much steeper density profile of blue cluster members compared to the red sequence galaxies. The higher relative abundance of blue galaxies in the outer region of rich clusters is well known from local morphological studies and deeper work with high resolution (Rines et al. 2000; Katgert et al. 2004; Postman et al. 2005) and is part of the general morphology-density relation (Dressler

1980). Such behaviour is commonly explained by the continued conversion of disk galaxies into S0 galaxies, via tidal and gas stripping processes (Abadi et al. 1999), and thought to be consistent with the observed evolution of the numbers of S0 galaxies relative to other cluster populations measured in the accessible redshift range  $z < 1$  (Dressler 1980; Ellis et al. 1997; Postman et al. 2005; Poggianti et al. 2009; Simard et al. 2009). Disk galaxies are expected to be relatively more affected than early-type objects as their stellar content is relatively less bound gravitationally and the gas is susceptible to ram pressure from the ICM.

In contrast, for early-type galaxies the  $M/L$  profile we obtained for each cluster is fairly flat, with only a shallow radial decline for  $r > 200h^{-1}$  kpc. Interestingly CDM based N-body simulations aimed at evaluating the tidal influence of the cluster potential do claim to predict a shallow radial decline in the ratio of cluster mass to the number of subhalos (Nagai & Kravtsov 2005; Reed et al. 2005; Natarajan et al. 2009), matching well our observed trend. The simulations indicate that although up to 70% of a galaxy halo mass can be stripped over a Hubble time for those objects with orbits bringing them close to the cluster centre, the stellar content is not likely to be significantly affected, at least for early-type galaxies, as the stars are more tightly bound. Hence, a relatively flat relation is expected reflecting the relatively collisionless behaviour of both galaxies and DM. Therefore, even though tidal effects are significant, the luminous component that we measure when examining the  $M/L$  profile of early-type galaxies is expected to be only slightly affected, in good agreement with the mild decline we observe for each cluster.

Further work on the tidal evolution of clusters is obviously needed. This is particularly important in view of the interesting tension that has now emerged between the relatively concentrated mass profiles measured for many high mass clusters, compared to the much shallower mass profiles predicted by standard  $\Lambda$ CDM (Duffy et al. 2008; Broadhurst et al. 2008; Oguri et al. 2009). Steeper mass profiles lead to stronger tidal effects and compounded with the greater ages implied by the relatively high concentrations should lead to more significant tidal effects. Measuring directly the tidal truncation of luminous cluster member galaxies should be feasible via lensing in favorable cases where multiple images are locally affected by individual halos. The statistical influence on the general lensing deflection field has been claimed to be detected for two clusters independently by Natarajan et al. (2009) for Cl0024+16 and by Halkola, Seitz & Pannella (2007) for A1689. These first results encourage further deeper work with an emphasis on the degree of correlation of the lensing signal with cluster member galaxies, a formidable challenge but one well worthy of pursuit.

## ACKNOWLEDGMENTS

We are grateful to N. Kaiser for making the IMCAT package publicly available. EM thanks Eran Ofek for his publicly available Matlab scripts, and Assaf Horesh and Ido Finkelman for useful discussions. We thank the anonymous referee for useful comments. Work at Tel-Aviv University was supported by Israel Science Foundation grant 214/02. This work was also supported in part by National Science Council of

Taiwan under the grant NSC95-2112-M-001-074-MY2.MO and supported by Department of Energy contract DE-AC02-76SF00515.

## REFERENCES

- Abadi M. G., Moore B., Bower R. G., 1999, MNRAS, 308, 947  
 Adami C., Ilbert O., Pelló R., Cuillandre J. C., Durret F., Mazure A., Picat J. P., Ulmer M. P., 2008, A&A, 491, 681  
 Adelman-McCarthy J. K., Agüeros M. A., Allam S. S., Allende Prieto C., Anderson K. S. J., Anderson S. F., Annis J., Bahcall N. A., et al., 2008, ApJS, 175, 297  
 Arieli Y., Rephaeli Y., Norman M. L., 2008, ApJ, 683, L111  
 Bardeau S., Kneib J.-P., Czoske O., Soucail G., Smail I., Ebeling H., Smith G. P., 2005, A&A, 434, 433  
 Benítez N., 2000, ApJ, 536, 571  
 Benítez N., Ford H., Bouwens R., Menanteau F., Blakeslee J., Gronwall C., Illingworth G., Meurer G., et al., 2004, ApJS, 150, 1  
 Bertin E., 2006, in Astronomical Society of the Pacific Conference Series, Vol. 351, Astronomical Data Analysis Software and Systems XV, Gabriel C., Arviset C., Ponz D., Enrique S., eds., pp. 112–+
- Bertin E., Arnouts S., 1996, A&AS, 117, 393  
 Blumenthal G. R., Faber S. M., Flores R., Primack J. R., 1986, ApJ, 301, 27  
 Bolzonella M., Miralles J.-M., Pelló R., 2000, A&A, 363, 476  
 Bravo-Alfaro H., Cayatte V., van Gorkom J. H., Balkowski C., 2000, AJ, 119, 580  
 Broadhurst T., Takada M., Umetsu K., Kong X., Arimoto N., Chiba M., Futamase T., 2005, ApJ, 619, L143  
 Broadhurst T., Umetsu K., Medezinski E., Oguri M., Rephaeli Y., 2008, ApJ, 685, L9  
 Broadhurst T. J., Barkana R., 2008, MNRAS, 390, 1647  
 Calzetti D., Kinney A. L., Storchi-Bergmann T., 1994, ApJ, 429, 582  
 Capak P., Aussel H., Ajiki M., McCracken H. J., Mobasher B., Scoville N., Shopbell P., Taniguchi Y., et al., 2007, ApJS, 172, 99  
 Clowe D., Schneider P., 2001, A&A, 379, 384  
 Coe D., Benítez N., Sánchez S. F., Jee M., Bouwens R., Ford H., 2006, AJ, 132, 926  
 Colín P., Klypin A. A., Kravtsov A. V., Khokhlov A. M., 1999, ApJ, 523, 32  
 Crawford S. M., Bershadsky M. A., Hoessel J. G., 2009, ApJ, 690, 1158  
 De Lucia G., Kauffmann G., Springel V., White S. D. M., Lanzoni B., Stoehr F., Tormen G., Yoshida N., 2004, MNRAS, 348, 333  
 Dressler A., 1980, ApJ, 236, 351  
 Duffy A. R., Schaye J., Kay S. T., Dalla Vecchia C., 2008, MNRAS, 390, L64  
 El-Zant A., Shlosman I., Hoffman Y., 2001, ApJ, 560, 636  
 Ellis R. S., Smail I., Dressler A., Couch W. J., Oemler A. J., Butcher H., Sharples R. M., 1997, ApJ, 483, 582  
 Fioc M., Rocca-Volmerange B., 1997, A&A, 326, 950  
 Gao L., White S. D. M., Jenkins A., Stoehr F., Springel V., 2004, MNRAS, 355, 819  
 Gavazzi R., 2005, A&A, 443, 793  
 Ghigna S., Moore B., Governato F., Lake G., Quinn T., Stadel J., 1998, MNRAS, 300, 146  
 —, 2000, ApJ, 544, 616  
 Gunn J. E., Gott J. R. I., 1972, ApJ, 176, 1  
 Halkola A., Seitz S., Pannella M., 2007, ApJ, 656, 739  
 Heymans C., Van Waerbeke L., Bacon D., Berge J., Bernstein G., Bertin E., Bridle S., Brown M. L., et al., 2006, MNRAS, 368, 1323

- Homeier N. L., Demarco R., Rosati P., Postman M., Blakeslee J. P., Bouwens R. J., Bradley L. D., Ford H. C., et al., 2005, *ApJ*, 621, 651
- Huertas-Company M., Foex G., Soucail G., Pelló R., 2009, *A&A*, 505, 83
- Ilbert O., Capak P., Salvato M., Aussel H., McCracken H. J., Sanders D. B., Scoville N., Kartaltepe J., et al., 2009, *ApJ*, 690, 1236
- Kaiser N., Squires G., Broadhurst T., 1995, *ApJ*, 449, 460
- Kashikawa N., Shimasaku K., Yasuda N., Ajiki M., Akiyama M., Ando H., Aoki K., Doi M., et al., 2004, *PASJ*, 56, 1011
- Katgert P., Biviano A., Mazure A., 2004, *ApJ*, 600, 657
- Kenney J. D. P., Tal T., Crowl H. H., Feldmeier J., Jacoby G. H., 2008, *ApJ*, 687, L69
- Kinney A. L., Calzetti D., Bohlin R. C., McQuade K., Storchi-Bergmann T., Schmitt H. R., 1996, *ApJ*, 467, 38
- Kneib J.-P., Hudelot P., Ellis R. S., Treu T., Smith G. P., Marshall P., Czoske O., Smail I., et al., 2003, *ApJ*, 598, 804
- Kotulla R., Fritze U., Weilbacher P., Anders P., 2009, *MNRAS*, 396, 462
- Kronberger T., Kapferer W., Ferrari C., Unterguggenberger S., Schindler S., 2008, *A&A*, 481, 337
- Lacey C., Cole S., 1993, *MNRAS*, 262, 627
- Lapi A., Cavaliere A., 2009, *ApJ*, 695, L125
- Limousin M., Richard J., Jullo E., Kneib J.-P., Fort B., Soucail G., Elfadlóttir Á., Natarajan P., et al., 2007, *ApJ*, 668, 643
- Limousin M., Sommer-Larsen J., Natarajan P., Milvang-Jensen B., 2009, *ApJ*, 696, 1771
- Lu T., Gilbank D. G., Balogh M. L., Milkeraitis M., Hoekstra H., Van Waerbeke L., Wake D. A., Edge A. C., et al., 2009, ArXiv e-prints
- Marvel K. B., Shukla H., Rhee G., 1999, *ApJS*, 120, 147
- Medezinski E., Broadhurst T., Umetsu K., Coe D., Benítez N., Ford H., Rephaeli Y., Arimoto N., et al., 2007, *ApJ*, 663, 717
- Miyazaki S., Komiyama Y., Sekiguchi M., Okamura S., Doi M., Furusawa H., Hamabe M., Imi K., et al., 2002, *PASJ*, 54, 833
- Moore B., Katz N., Lake G., Dressler A., Oemler A., 1996, *Nature*, 379, 613
- Nagai D., Kravtsov A. V., 2005, *ApJ*, 618, 557
- Natarajan P., Kneib J.-P., Smail I., Treu T., Ellis R., Moran S., Limousin M., Czoske O., 2009, *ApJ*, 693, 970
- Natarajan P., Loeb A., Kneib J.-P., Smail I., 2002, *ApJ*, 580, L17
- Navarro J. F., Frenk C. S., White S. D. M., 1997, *ApJ*, 490, 493
- Oguri M., Blandford R. D., 2009, *MNRAS*, 392, 930
- Oguri M., Hennawi J. F., Gladders M. D., Dahle H., Natarajan P., Dalal N., Koester B. P., Sharon K., et al., 2009, *ApJ*, 699, 1038
- Okabe N., Takada M., Umetsu K., Futamase T., Smith G. P., 2009, ArXiv e-prints
- Ouchi M., Shimasaku K., Okamura S., Furusawa H., Kashikawa N., Ota K., Doi M., Hamabe M., et al., 2004, *ApJ*, 611, 660
- Poggianti B. M., Fasano G., Bettoni D., Cava A., Dressler A., Vanzella E., Varela J., Couch W. J., et al., 2009, *ApJ*, 697, L137
- Popesso P., Biviano A., Böhringer H., Romaniello M., 2006, *A&A*, 445, 29
- Postman M., Franx M., Cross N. J. G., Holden B., Ford H. C., Illingworth G. D., Goto T., Demarco R., et al., 2005, *ApJ*, 623, 721
- Reed D., Governato F., Quinn T., Gardner J., Stadel J., Lake G., 2005, *MNRAS*, 359, 1537
- Rines K., Geller M. J., 2008, *AJ*, 135, 1837
- Rines K., Geller M. J., Diaferio A., Kurtz M. J., Jarrett T. H., 2004, *AJ*, 128, 1078
- Rines K., Geller M. J., Diaferio A., Mohr J. J., Wegner G. A., 2000, *AJ*, 120, 2338
- Sadeh S., Rephaeli Y., 2008, *MNRAS*, 388, 1759
- Schechter P., 1976, *ApJ*, 203, 297
- Schindler S., Kapferer W., Dominko W., Mair M., van Kampen E., Kronberger T., Kimeswenger S., Ruffert M., et al., 2005, *A&A*, 435, L25
- Simard L., Clowe D., Desai V., Dalcanton J. J., von der Linden A., Poggianti B. M., White S. D. M., Aragón-Salamanca A., et al., 2009, *A&A*, 508, 1141
- Springel V., White S. D. M., Tormen G., Kauffmann G., 2001, *MNRAS*, 328, 726
- Umetsu K., Birkinshaw M., Liu G.-C., Wu J.-H. P., Medezinski E., Broadhurst T., Lemze D., Zitrin A., et al., 2009a, *ApJ*, 694, 1643
- Umetsu K., Broadhurst T., 2008, *ApJ*, 684, 177
- Umetsu K., Medezinski E., Broadhurst T., Zitrin A., Okabe N., Hsieh B., Molnar S. M., 2009b, ArXiv e-prints
- Vollmer B., Beck R., Kenney J. D. P., van Gorkom J. H., 2004, *AJ*, 127, 3375
- Wuyts S., Franx M., Cox T. J., Hernquist L., Hopkins P. F., Robertson B. E., van Dokkum P. G., 2009, *ApJ*, 696, 348
- Yagi M., Kashikawa N., Sekiguchi M., Doi M., Yasuda N., Shimasaku K., Okamura S., 2002, *AJ*, 123, 66
- Zacharias N., Monet D. G., Levine S. E., Urban S. E., Gaume R., Wycoff G. L., 2004, in *Bulletin of the American Astronomical Society*, Vol. 36, *Bulletin of the American Astronomical Society*, pp. 1418–+
- Zitrin A., Broadhurst T., Umetsu K., Coe D., Benítez N., Ascaso B., Bradley L., Ford H., et al., 2009, *MNRAS*, 396, 1985